Simulation and experimental study of remote field current testing for hidden defects of aluminum alloy plate with damping coating

Shichao Jiang, Xinliang Lu and Hongliang Wang
State-owned Wuhu Machinery Factory, Wuhu, China, and

Kai Song and Yuanyuan Jiang
Key Laboratory of Nondestructive Testing, Ministry of Education, Nanchang Hangkong University, Nanchang, China

Abstract

Purpose – Detection of hidden defects of aluminum alloy plate with damping coating is a challenging problem. At present, only a few non-destructive testing methods exist to address this engineering problem. Without the restriction of skin effect, remote field eddy current (RFEC) overcomes the interference caused by the damping coating. The RFEC, which has potential advantages for detecting the hidden defects of aluminum plate with damping coating, can penetrate the metal plate to detect buried depth defects. This study aims to test how thick the RFEC sensor can penetrate the metal plate to detect the buried defects.

Design/methodology/approach – The magnetic field distribution characteristics are analyzed, the magnetic field intensity distribution is calculated, and the structure and parameters of the coil, magnetic circuit and shielding damping are determined through the two- and three-dimensional finite element simulation methods. Optimal excitation frequency is obtained, and the distance between the excitation coil and detection coil is determined by analyzing the relationship between excitation frequency and remote field points.

Findings – Simulation and experimental results verify the feasibility of applying the RFEC detection technology in detecting the hidden defects of aluminum alloy plate with damping coating.

Originality/value – In this paper, the RFEC testing model of hidden defects in aluminum plate sample with damping coating is established by using the finite element method.

Keywords Damping coating, Hidden defect, Remote field eddy current, Finite element simulation

Paper type Research paper

1. Introduction

The rail vehicle bottom aluminum alloy plate works because of long-term adverse conditions, such as heat, alternating stress and corrosive media; as a result, stress and fatigue corrosion cracks, which seriously threaten the safe operation of a vehicle, are easily generated on the back of the aluminum alloy plate (Pokhmurskii *et al.*, 2011; Woo *et al.*, 2010). Therefore, the early detection of these cracks is essential to prevent any accidents that can cause loss of life. The plate surface is covered with a 5 mm-thick damping coating sound-absorbing material based on pure acrylic emulsion (Yano *et al.*, 2019). The damping coating surface is rough. Moreover, the space around the back of the aluminum alloy plate is narrow, thereby preventing detection. Poor working conditions lead to daily in-service maintenance and abrasive overhaul cannot be carried out smoothly. Therefore, breaking through the 5 mm-thick damping coating interference and the in-service inspection of hidden defects of aluminum alloy plate are engineering problems with research significance and needs to be solved urgently.

At present, scholars have conducted numerous of research and experiments on the in-service detection of metal specimens with damping coating. Dalton *et al.* (2009) used an infrared scanning system to examine the surface crack of steel under black paint by analyzing the influence of cracks and heat flow directions on the testing results. Wang *et al.* (2019) used induction thermal imaging to detect the natural crack on the surface of forgings under a 0.5 mm-thick paint coating. However, these studies only focused on the surface defects of the testing specimens and only considered the damping coating

with less than 5 mm thickness. So far, the detection of thicker damping coating and non-surface defects has only relied on ultrasound and X-ray detection technology. In the research of this subject, the ultrasonic energy will be severely attenuated and cannot be completed because the damping coating is a sound-absorbing and noise-reducing material (Fan *et al.*, 2009). X-ray detection technology is not used because it requires the use of large equipment, and the ray source used for the detection can cause harm to the human body when no protective measures, such as leaded walls, are used (Du Plessis *et al.*, 2016; Askari *et al.*, 2019). In addition, pulse eddy current technology (Sophian *et al.*, 2017) is not used. Therefore, the introduction of a convenient and reliable detection technology is needed to complete the detection of aluminum alloy plate with damping coating.

Remote field eddy current (RFEC) testing (RFECT) technology is an indispensable part of electromagnetic nondestructive testing because its unique advantages are not affected by the skin effect and have the capacity to test specimens twice through electromagnetic field penetration. The conventional RFECT mainly applied in the detection of ferromagnetic pipelines (Shi *et al.*, 2019a, 2019b; Robinson, 1998; Thirunavukkarasu *et al.*, 2008; Fukutomi *et al.*, 2001; Shi *et al.*, 2019a, 2019b; Xiao *et al.*, 2018; She *et al.*, 2021) achieved the best optimization effect by introducing a shielding plate between the excitation and detection coils and a ferromagnetic ring outside the ferromagnetic pipeline. Some people have proposed remote on-site eddy current probes for on-the-job inspections of pipeline defects (Xu *et al.*, 2019). RFECT has a significant penetration ability for rough welding areas on pipelines and has been used to detect deeper hidden cracks (Xie *et al.*, 2018). Jayaraman *et al.* (2021) rely on RFEC technology to develop three-dimensional (3D)numerical models for steam generator tubes. In recent years, RFECT technology has been widely used in the detection of hidden defects in flat specimens. Sun *et al.* (2008) conducted numerical simulations on the generation and characteristics of RFEC in conductive plates and proposed the idea of controlling and guiding energy flow through magnetic circuits and combined shielding. Chen and Huang (2017) designed a different-axis planar RFEC sensor by placing the excitation and detection coils at a certain distance. The test results showed that the sensor responds to the flat-bottom hole defect of Φ10. However, the sensitivity of the sensor has not been investigated further. Ona *et al.* (2019) improved the detection capability by optimizing the gap of the coil inside the sensor. Kasai *et al.* (2011) designed the U-type component-based sensor to extend the RFEC further in the detection of back-side flaw in multilayer boards. Yang *et al.* (2017a, 2017b) developed a RFEC sensor that was suitable for riveted structures. Yang *et al.* (2017a, 2017b) based their study on the aspects of signal enhancement and magnetic field suppression. For on-site inspection of hidden cracks along the plane riveting rivet holes, a team established a finite element model for remote on-site eddy current inspection of hidden cracks in multilayer metal riveting members (Zhao *et al.*, 2020). However, in this research, the magnetic field infiltrated into the test specimens is frail because of the large thickness of the damping coating.

In this paper, ANSYS simulation software is used to establish a 3D finite element (Kermadi *et al.*, 2018; Yang and Yoon, 2001) simulation model for the RFECT of aluminum plate specimens with damping coating. The magnetic circuit and magnetic field shielding structure of planar RFEC sensor are optimized systematically. The planar RFEC sensor is designed and fabricated. The experimental research on the hidden crack defects (He *et al.*, 2011) of the aluminum plate with damping coating is conducted. The research shows that RFECT can detect the hidden crack defects of the aluminum plate with damping coating effectively and expand the application field RFEC detection technology.

2. Detection principle

Before studying the mechanism of flat far-field eddy current detection, we must first analyze the principle of far-field eddy current in the pipeline. For the conventional far field eddy current testing method, the excitation coil and the detection coil are placed coaxially inside the pipe and are coaxial with the pipe (Figure 1). The excitation coil is loaded with a low-frequency sinusoidal signal to generate a low-frequency excitation magnetic field. Due to the shielding effect of the

Figure 1 Traditional RFEC principle
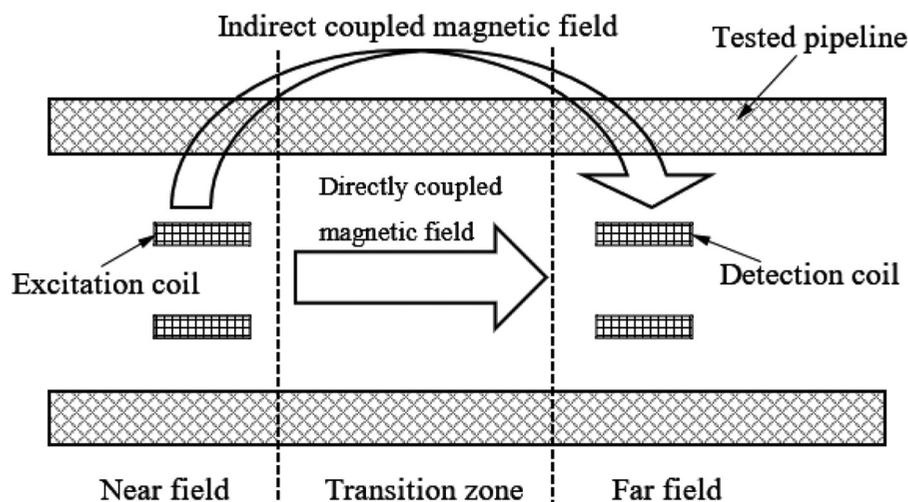
pipeline, the direct coupling magnetic field is fast Attenuation, the indirect coupling magnetic field penetrates the tube wall twice to reach the detection coil. The distance between the detection coil and the excitation coil is generally 2–3 times the tube diameter.

When the distance between the detection coil and the excitation coil is 0 to 1.5, the amplitude of the far-field eddy current detection signal attenuates sharply. This area is usually called the "near-field area" of the far-field eddy current; in the range of 1.5 to 2.5 times the pipe diameter, the detection signal amplitude has an "inflection point" and the phase has a 90° reversal. This area is called the "transition zone"; continue to increase the axial distance between the detection coil and the excitation coil, and the detection signal the amplitude and phase changes tend to be flat, indicating that it is already in the far-field eddy current detection area.
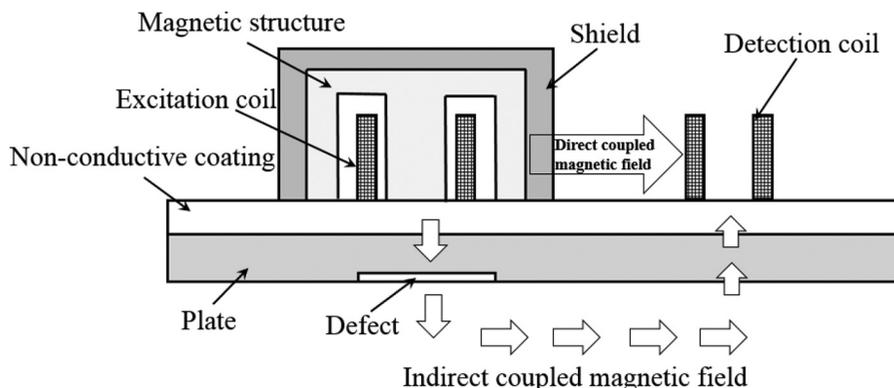
The planar RFEC sensor is composed of excitation/ detection coil, magnetic collecting structure and magnetic field shield structure. Compared with the coaxial arrangement of the excitation/detection coil of the traditional RFEC sensor, the planar RFEC sensor adopts the different-axis placement mode (Figure 2). In the experiment, excitation coil generates alternating magnetic field. The magnetic collecting structure can enhance the excitation magnetic field and guide the magnetic field to penetrate the aluminum plate specimen. The shield structure effectively blocks the direct coupling magnetic field from reaching the detecting coil and prevents the detection signal amplitude from being saturated quickly.

The indirect coupled magnetic field penetrates aluminum plate specimens twice and thus carry the health status information of aluminum plate. The detection coil receives indirect coupled magnetic field in the remote field region, which penetrates aluminum plate specimen twice. The magnetic field generates voltage signal through the detection coil. Thus, magnetic field lines are distorted when defects exist in an aluminum plate. Subsequently, the detection signal amplitude fluctuates so that RFECT effectively detects the presence or absence of defects.

The governing equations for RFEC can be derived from Maxwell's equations as follows:

$$\nabla^2 \vec{A} = -\mu \vec{J_s} + j\omega\sigma\mu\vec{A} \tag{1}$$

Where A is the magnetic vector potential, $\vec{J_s}$ is the current density, σ is the dielectric constant and μ. is the magnetic permeability. The equation illustrates that the electromagnetic field propagates in the form of waves. The 3D problem is simplified into a two-dimensional (2D) problem because the excitation module is a columnar structure. Equation (1) can be rewritten as:

$$\frac{\partial^2 \vec{A}}{\partial r^2} + \frac{1}{r}\frac{\partial \vec{A}}{\partial r} + \frac{\partial^2 \vec{A}}{\partial z^2} - \frac{\vec{A}}{r^2} = -\mu\vec{J_s} + j\omega\sigma\mu\vec{A} \tag{2}$$

In the formula, the eddy current density d the magnetic vector position $\vec{A}$ are symmetrical axes of the z-axis, which constitute a function of r and z. No external excitation current in the plate exists in the RFEC model, thus, $\vec{J_s}$ = 0. Then, the aforementioned formula can be changed into:

$$\frac{\partial^2 \vec{A}}{\partial r^2} + \frac{1}{r}\frac{\partial \vec{A}}{\partial r} + \frac{\partial^2 \vec{A}}{\partial z^2} - \frac{\vec{A}}{r^2} - j\omega\sigma\mu\vec{A} = 0 \tag{3}$$

The induced voltage of the detection coil can be obtained by Faraday's electromagnetic induction law as:

$$U = j\,\omega\,\frac{2\pi N}{A}\int_{r_1}^{r_2}\int_0^h rA(r,z)d_z d_r \tag{4}$$

Where N is the number of turns of the coil, A is the cross-sectional area of the coil and r is the radial distance from the coil.

The induced voltage of the detection coil refers to the measured voltage. The solution of the equation can be calculated using ANSYS finite element simulation software. Therefore, the defect form can be characterized by the change in voltage amplitude.

3. Design of remote field eddy current sensor

3.1 Establishing remote field eddy current simulation model with damped aluminum plate

The RFECT model of 3D finite element damped aluminum plate buried crack has been simulated and established by using the finite element simulation software, ANSYS. The simulation

Figure 2 Plane RFEC principle

model is mainly composed of an aluminum plate, a RFEC sensor, a damping coating and air. Figure 3 shows the model profile. The damping coating is evenly distributed on the aluminum plate surface, and the crack defect is located at the center of the back of the aluminum plate. The excitation/detection coil is placed symmetrically on the crack defect. The sensor scans the defect parallel to the length of the defect. The material properties and dimensions used in the simulation model are listed in Table 1.

3.2 Sensor coil design

Excitation coil is a core component of the RFEC sensor. Its designed size directly affects the magnitude of the excitation magnetic field. Thus, the inner diameter of the excitation coil is investigated initially. Given that the model only contains the aluminum plate and the excitation coil, the whole model is axisymmetric, that is, it does not involve relative motion. Therefore, the 2D simulation model can be used to analyze the distribution of magnetic lines in the aluminum plate

member, the relationship between the inner diameter of the coil and the strength of the magnetic field. To test the validity of different inner diameter of the exciting coil, the inner diameter of the excitation coil is set to 2 mm and 8 mm, the wall thickness is set as 1 mm, the height is set as 4 mm, the number turns is 600, the excitation frequency is 600 Hz and the excitation current is 100 mA. The simulation results are illustrated in Figure 4.

The characteristics of magnetic field lines of the 2 mm and 8 mm inner diameter excitation coils in the aluminum plate are shown in Figure 4. Apparently, the magnetic flux density of excitation coil inner diameter is larger by 8 mm than the excitation coil with an inner diameter of 2 mm. Therefore, the increase in the inner diameter of the excitation coil enhances the excitation magnetic field. Furthermore, the specific relationship between the inner diameter of the coil and the strength of the magnetic field is analyzed. Figure 5 shows the extraction of the magnetic field strength in the aluminum plate under the excitation coil with inner diameters of 2, 4, 6 and 8 mm.
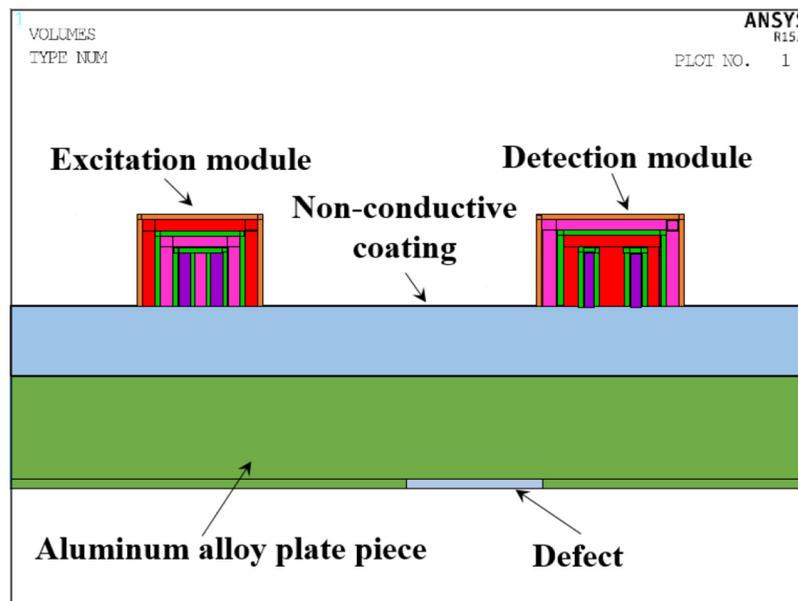
Figure 3 3D simulation model diagram

**Table 1** Material properties and dimensions

Conductivity of the aluminum plate (MSm^{-1})	25.5	Relative magnetic permeability	1
Length, width, and thickness of the plate (mm)	300 150	Thickness of the damping coating (mm)	5
The thickness of the exciting coil (mm)	1	Number of turns of the exciting coil	600
Wall thickness, inner length, inner width of the detection coil (mm)	1 2 4	Number of turns of the exciting coil	800
Conductivity of the copper shield (MSm^{-1})	58.8	Relative magnetic permeability	1
Conductivity of the magnetic circuit (MSm^{-1})	0.005	Relative magnetic permeability	1×10^4
Frequency of excitation (Hz)	600	Current of excitation (mA)	100

Figure 4 Magnetic flux distribution of excitation coils with different inner diameters

(a)   **(b)**
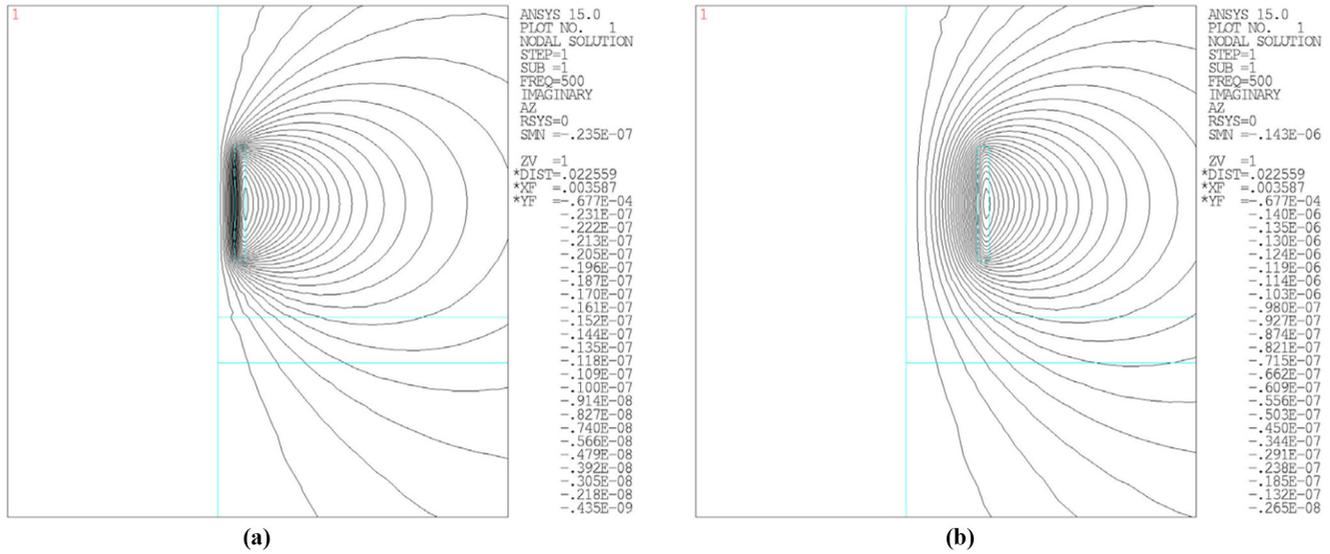
Notes: (a) 2 mm inner diameter; (b) 8 mm inner diameter

Figure 5 Relationship between the inner diameter of the excitation coil and the magnetic field intensity
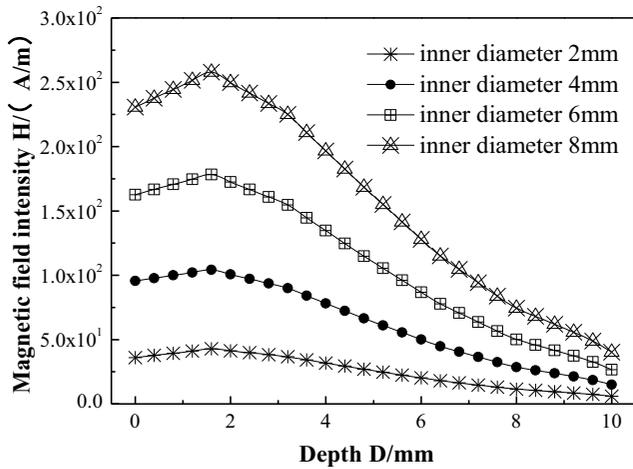
The magnetic field strength generated by excitation coils with different inner diameters consistently decreases within a range of 2 mm to 10 mm of the aluminum plate. Figure 5 shows that the magnetic field strength is proportional to the inner diameter of the coil at the same depth. Therefore, increasing the inner diameter of the coil enhances the magnetic field strength that penetrates the aluminum plate specimen and improves detection sensitivity. However, in the actual detection process, increasing the inner diameter of the excitation coil is not conducive to the detection of cracks with small length. As a result, this test selects an excitation coil with an inner diameter of 8 mm to detect crack length.

The coil height is changed to 4, 5, 6 and 7 mm; the effect of the excitation coil height on the magnetic field strength of the aluminum plate is investigated, and the magnetic field strength in the aluminum plate under the excitation coil is extracted on the basis of the excitation coil with 8 mm inner diameter. The results are expressed in Figure 6.

In Figure 6, the strength of the magnetic field decreases as the coil height increases. The increase in coil height causes the magnetic lines to be mainly concentrated on the bottom face of the coil. Therefore, the magnetic force that permeates the aluminum plate specimen is reduced. The coil size with 8 mm inner diameter and 4 mm height must be confirmed for the next study to enhance the magnetic field strength and ensure high sensitivity according to the aforementioned analysis and explanations.

The aforementioned studies show that the magnetic lines of force generated by the excitation coil are very divergent, thereby causing the energy of the magnetic field in the aluminum plate to be insufficient. Therefore, the magnetic circuit structure is designed according to the magnetic lines of force distribution characteristics of the coil to guide the

Figure 6 Relationship between excitation coil height and magnetic field intensity
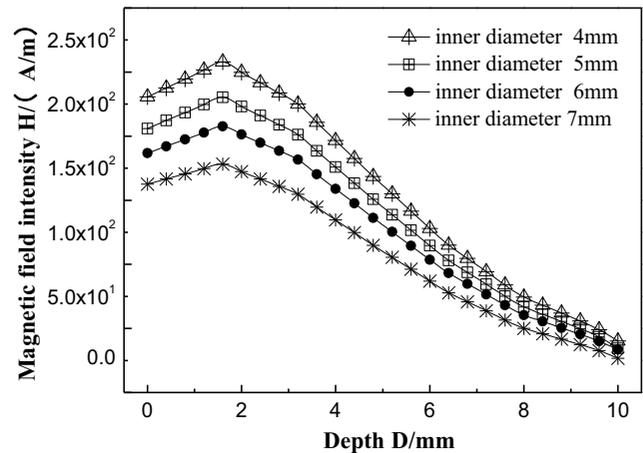
magnetic lines of force and to improve the magnetic field strength in an aluminum plate.

In Figure 7(a), the magnetic lines of force are closed and curved and pass through the inner diameter of the coil, in which density increases from the center of the coil to the inner wall. Figure 7(b) shows that the bottom surface of the coil corresponds to the region with the most reliable magnetic field strength, and the strength of the magnetic field gradually decreases from the inner wall to the external wall of the coil.

Figure 8 shows the magnetic circuit design patterned from the magnetic line trajectory generated by the excitation coil, which includes a central magnetic column and a peripheral magnetic cup. Figure 9 shows the placement of the excitation coil in sectional view. The magnetic column radius is d_1, and the magnetic cup wall thickness is $d_2 = d_3$. The air gap between the inner wall of the excitation coil and the magnetic column is r_3. The air gap $r_1 = r_2$ is placed between the magnetic cup and the excitation coil.

To further enhance the magnetic field strength in the aluminum plate, the magnetic field line is propagated using ferrite guide. Ferrite magnetic permeability is μ_1 and μ_1 μ_{air}. The induced magnetic field strength in the magnetic circuit is represented as B. Induced magnetic field strength is expressed as B = μ_{1H}.

First, the relationship of magnetic field strength with different sizes is established in terms of the magnetic cylinder diameter. The size of the excitation coil is kept constant. The radius d_1 of the magnetic cylinder is changed to 1.5, 2, 2.5, 3 and 3.5 mm. The relationship of magnetic field strength in the aluminum plate and the diameter size of the magnetic cylinder is investigated. The magnetic field is extracted from the aluminum plate under the excitation coil. The results are shown in Figure 10.

The results show that the magnetic field strength in the aluminum plate is proportional to the magnetic cylinder radius. The increase in radius d_1 of the magnetic cylinder causes the air

gap r_3 The air gap between the magnetic cylinder and the inner wall of the coil decreases, thereby increasing the magnetic flux density in the magnetic cylinder. As a result, the induced magnetic field strength B increases, then the excitation magnetic field strength is increased.

Furthermore, a 2D finite element simulation model is established by keeping the magnetic cylinder radius d_1, the magnetic cup wall thickness d_2, d_3 unchanged and by changing the air gap size of r_1, r_2, which is between the magnetic cap and the coil, and by observing that the magnetic lines distribution with air gap size is $r_1 = r_2 = 1\,mm$ and $r_1 = r_2 = 4\,mm$. The result is shown in Figure 11.

When the air gap between the inner wall of the magnetic cup and the coil is $r_1 = r_2 = 1\,mm$, the magnetic lines of force mainly concentrated on the bottom surface of the coil. The magnetic flux density in the aluminum plate specimen is weak. When the air gap between the magnetic cap and the coil is $r_1 = r_2 = 4\,mm$, the magnetic flux density in the aluminum plate increases. The result is shown in Figure 11. The widening of air gaps increased the radius of the magnetic lines. Thus, more magnetic lines of force permeate the aluminum plate.

The air gap between the excitation coil and the inner wall of the magnetic cup is set to 0.5, 1, 1.5, 2.5 and 4 mm to determine the size of the air gap further. Subsequently, the magnetic field strength at different depths under the coil are extracted. The result is shown in Figure 12.

In Figure 12, increasing the air gap between the inner wall of the magnetic cup and the coil wall increases the magnetic field strength under the coil and can be improved in the specimen without changing the coil size. However, considering that the sensor size should not be too large during the actual detection process, the air gap of the inner wall of the magnetic cup is set to 2.5 mm for further research.

**Figure 7** Magnetic field distribution characteristics of the excitation coil

(a)

(b)
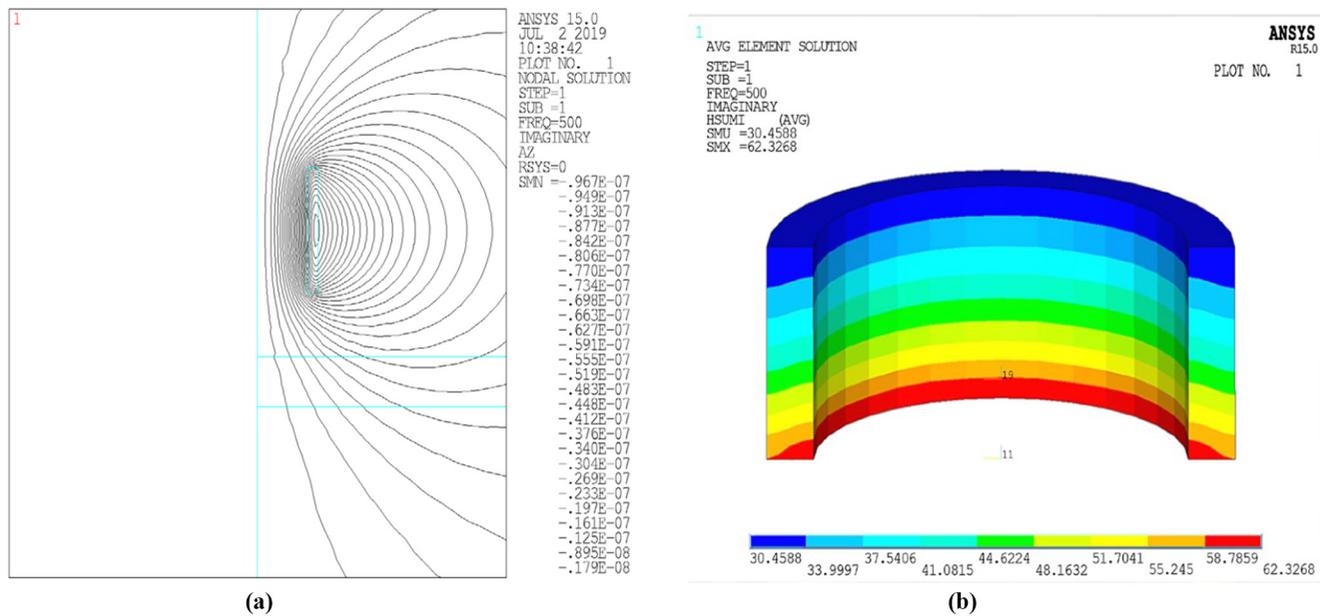
Notes: (a) Characteristics of magnetic lines; (b) magnetic field strength distribution

Figure 8 Magnetic circuit model structure
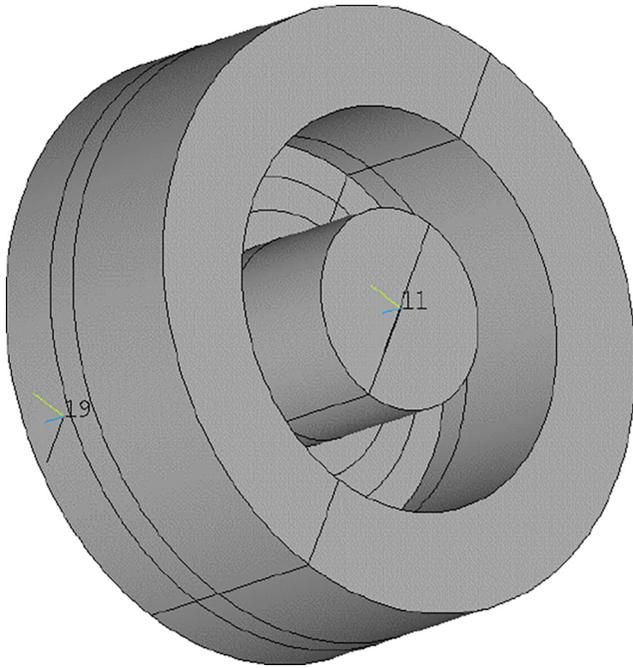
Figure 9 Schematic of magnetic circuit placement
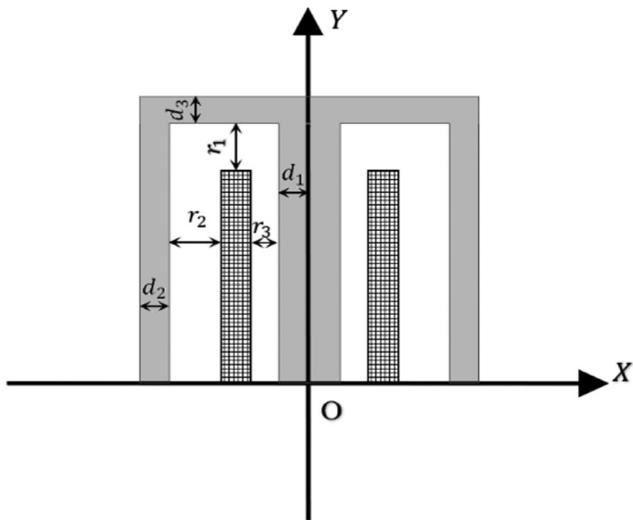
### 3.3 Shielding structure optimization

Regardless of whether the shielding damping is installed, the magnetic field strength decays continuously along the radial direction of the excitation coil. After the shielding damping is installed, the attenuation amplitude of the magnetic field strength is larger, and the magnetic field shielding performance of the composite shielding damping is relatively good. When the direct coupling channel energy passes through the aluminum–copper composite shielding damping, the magnetic field strength is the weakest and the direct coupling signal can be ignored, in other words, the direct coupling signal is shielded. The magnetic shielding performance is optimal at this time. The effect of shielding damping is shown in Figure 13.

Figure 10 Relationship between magnetic cylinder radius and magnetic field strength
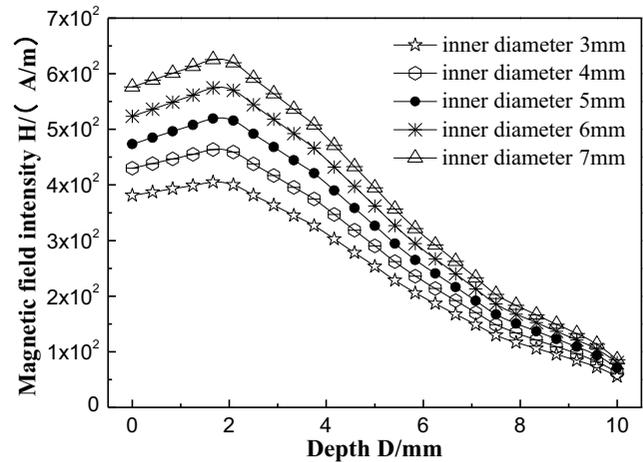
A cup-shaped shield that hinders the direct coupling magnetic field is designed to suppress the direct coupling magnetic field and shorten the distance between the excitation coil with the detection coil. The installation of shielding damping can quickly attenuate the magnetic field energy of the direct coupling channel, shorten the coil spacing and further reduce the size of the probe. Thus, a material with small magnetic permeability μ and large electrical conductivity σ as shield structure is selected. The induced electromotive force E_0 generates the magnetic field B_0, which penetrates the shielding structure. Thus, the electromotive force E_0 also increases with electric conductivity σ because $J_0 = \sigma E_0$. The same size of the shield structure can produce significant eddy current density J_0. The reverse magnetic field strength B_1 satisfies $\nabla \times B_1 = J_0 + \frac{\partial D_0}{\partial t}$. Thus, when the shield structure conductivity σ is large, the reverse magnetic field B_1 generated by the eddy current is strong. The magnetic field strength B_{vector} in the shield has a small structure, thereby satisfying the $B_{\text{vector}} = B_0 - B_1$ and achieving a remarkable shield effect. Therefore, copper with conductivity $\sigma = 57 \times 10^6 \text{S}/m$ and magnetic permeability $\mu = 4\pi \times 10^{-7} \text{H}/m$ is selected as the shield material. The wall thickness of the structure is set to 1, 4, and 6 mm to optimize the size of the copper cup wall thickness. Thereafter, shield capacity is measured. The magnetic field strength horizontal component of the aluminum plate surface is extracted. The response curves of the phase and amplitude are obtained. The result is shown in Figure 14.

The simulation result in Figure 14(a) shows that the amplitude decreases slowly from the center of the excitation coil in the region measuring 30 mm. In this region, the magnetic field strength of the aluminum plate surface is inversely proportional to the thickness of the shield structure, and the trend of the magnetic field strength is similar. Furthermore, increasing the thickness of the shield structure can shorten the distance between the "phase canyon" and the center of the excitation coil, but the phase tends to be gentle at 30 mm from the center of the excitation coil, which illustrates the remote field point of the eddy current [Figure 14(b)]. In summary, increasing the thickness of the shield structure

Figure 11 Magnetic field line diagram

(a)

(b)
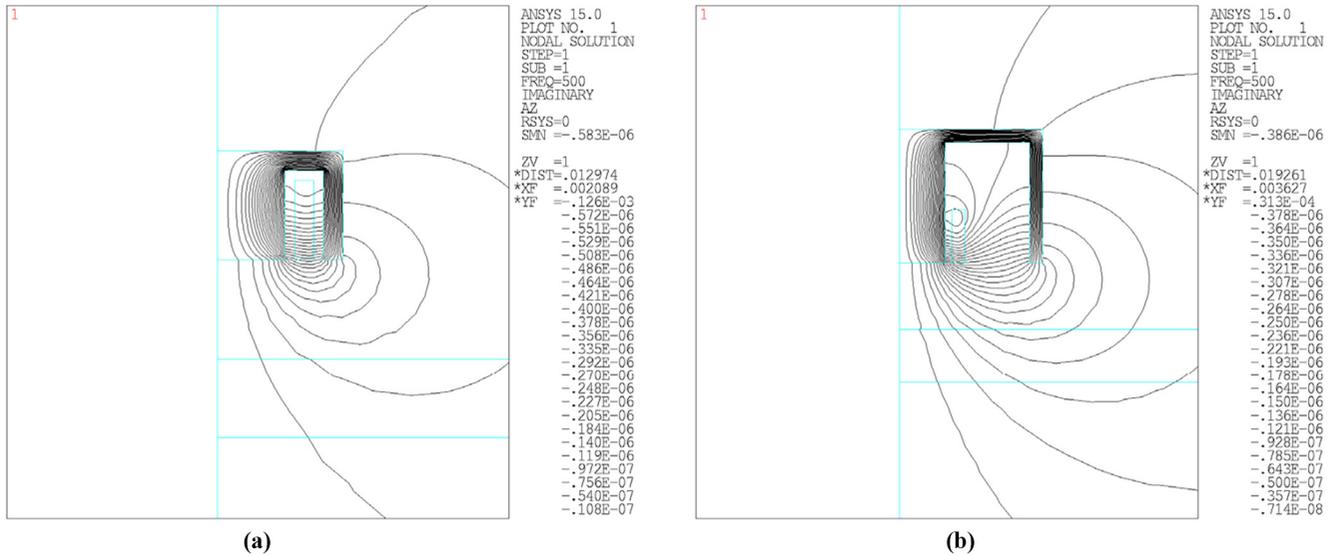
Notes: (a) $r_1 = r_2 = 1$mm; (b) $r_1 = r_2 = 4$mm

Figure 12 Relationship between the air gap and the magnetic field strength

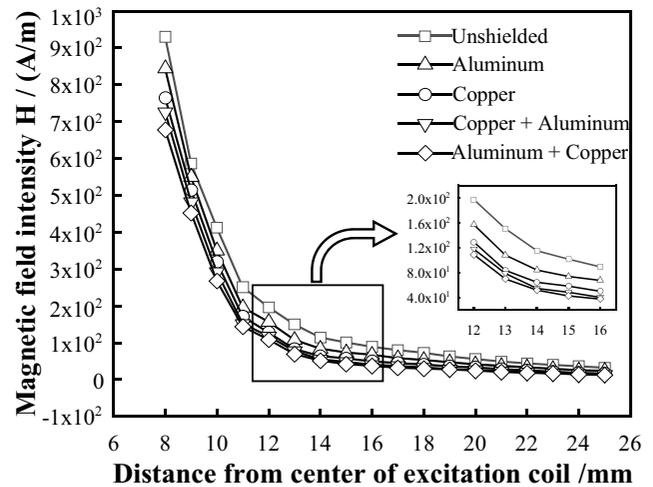
Figure 13 Comparison of shielding performance
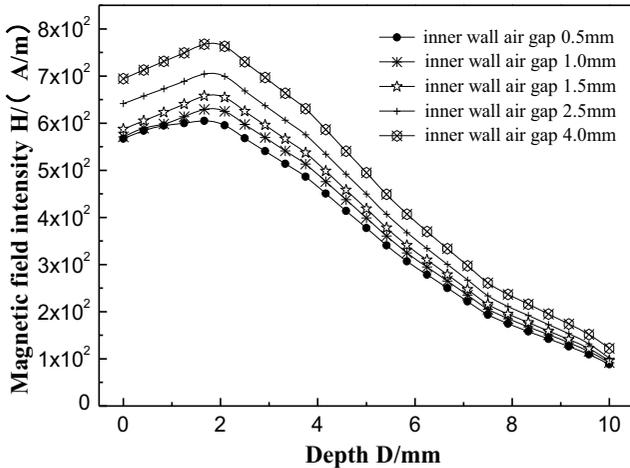
cannot shorten the distance between the distant field point and the center of the excitation coil effectively. However, increasing the thickness of the shield structure weakens the magnetic field strength in the remote field region, thereby decreasing detection sensitivity. Therefore, the copper cup with 1 mm thickness is selected as the shield structure.

### 3.4 Excitation signal frequency optimization

The excitation frequency not only affects the sensitivity of the RFEC detection but also the distance between the remote field point and the excitation coil in the RFEC detection process. The location of the remote field point at different excitation frequencies must be investigated to make the detection coil in the remote field region of the eddy. The excitation current is set to 100 mA based on the above simulation model. The

excitation frequency range is 100 Hz to 1 kHz. Simulation is performed every time 100 Hz is added. Thee magnetic field amplitude and phase of the aluminum plate surface are extracted at different excitation frequencies (Figure 15).

Figure 15(a) shows that in the excitation frequency range of 200 Hz to 1 kHz, the variation of the amplitude curve of magnetic field strength is consistent, that is, an "inflection point" within the range of 18 mm to 28 mm from the center of the excitation coil is exhibited. When departing from the center of the excitation coil larger than 30 mm, the amplitude characteristic curve decreases slowly, and the magnetic field strength is inversely proportional to the excitation frequency. Figure 15(b) shows that the increase in the excitation frequency can shorten the distance between the remote field point and the center of the excitation coil. Moreover, the phase characteristic

Figure 14 Characteristic curve of different shields
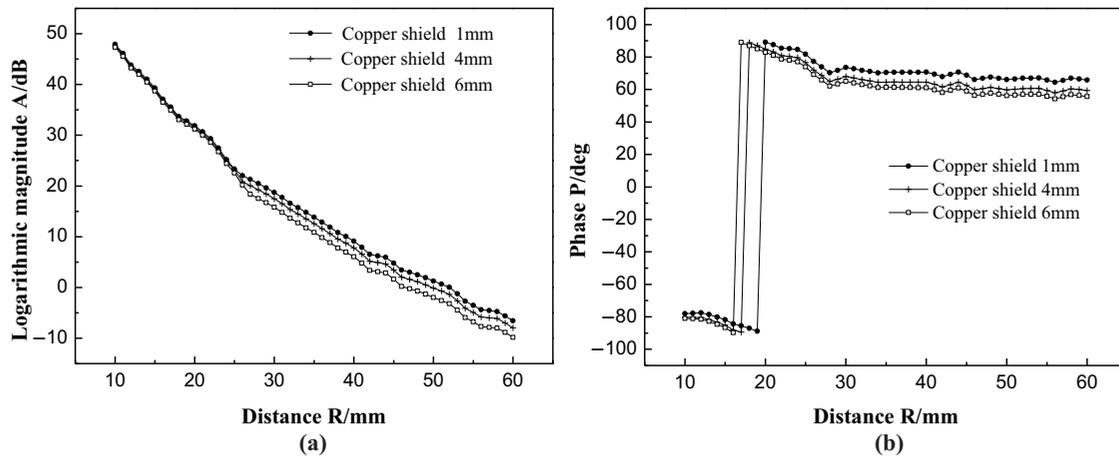
Notes: (a) Amplitude characteristic curve; (b) Phase characteristic curve

Figure 15 RFEC characteristics of different frequencies
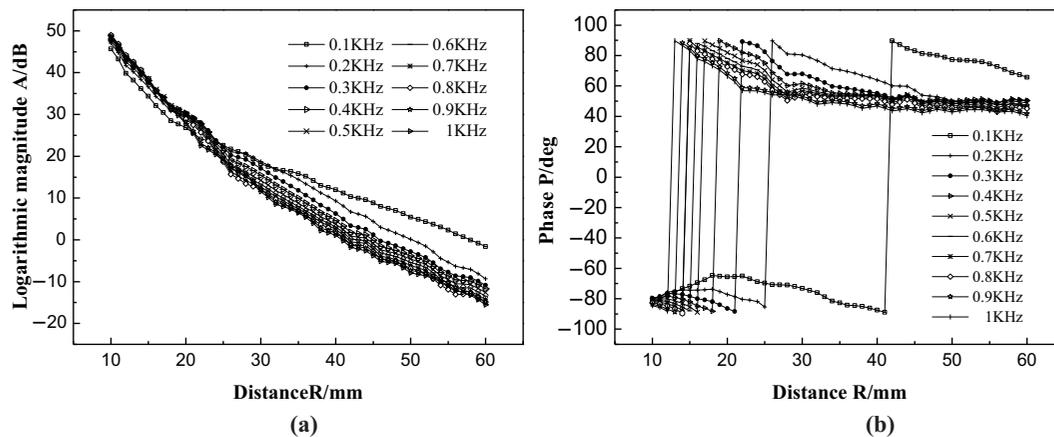
Notes: (a) Amplitude characteristic curve; (b) phase characteristic curve

curve changes slightly when departing from the center of the excitation coil to more than 30 mm. Thus, the remote field region is located at a distance greater than 30 mm from the center of the excitation coil. The position of the "phase canyon" tends to be stable when the excitation frequency is greater than 500 Hz. If the excitation frequency is high, then the signal amplitude decreases, thereby reducing detection sensitivity. Therefore, the excitation frequency is set to 600 Hz, and the optimized detection coil is placed at 30 mm from the center of the excitation coil.

4. Simulation and experimental analysis

4.1 Simulation results

In the process of finite element analysis for the 3D model, the SOLID62, SOLID97 and SOLID117 elements provided by ANSYS simulation software can be used for electromagnetic field analysis. Among them, only the SOLID97 element has the current coupling capability, does not contain intermediate nodes and has low requirements for computer performance. An eight-node hexahedral element is selected to model the

aluminum alloy floor, damping slurry, excitation/detection coil and near-field air. The element types and real constant settings are shown in Table 2.

To analyze the detection capability of the sensor, establishing a RFEC simulation model with the simulation data of the sensor and detection parameters detecting cracks on the backside of the damped aluminum plate. The defect model is 10 mm length × 0.2 mm width × 1 mm depth. The thickness of the plate is 1, 3, 5, and 8 mm. Moreover, the thickness of the damping coating is 5 mm, the excitation current is 100 mA and the excitation frequency is 600 Hz. During the detection, the sensor is parallel to the crack scanning, and the scanning method is shown in Figure 16. Sampling is conducted at the front of the sensor at a distance of 10 mm from the crack starting position. Stop sampling is conducted when the sensor leaves the crack at 10 mm. The simulation result is extracted every 1 mm.

Figure 17 illustrates that the crack detection signal amplitude is inversely proportional to the thickness of the aluminum plate. As the sensor approaches the defect, the signal amplitude

Table 2 Element types and real constants

| Physical area	Unit type	Unit options	Real constant
Aluminum alloy floor	SOLID97	KEYOPT(1) = 1	—
Coating	SOLID97	KEYOPT(1) = 1	—
Coil	SOLID97	KEYOPT(1) = 3	CARE, TURN, VOLU
Near field air	SOLID97	KEYOPT(1) = 0	—
Far field air	INFIN111	KEYOPT(1) = 1	—
Independent Current Source	CIRCU124	KEYOPT(1) = 3	R1 electrical amplitude R2 phase
Twisted coil	CIRCU124	KEYOPT(1) = 5	R1 symmetry factor
Resistance	CIRCU124	KEYOPT(1) = 0	R1 resistance value

Figure 16 Scanning method
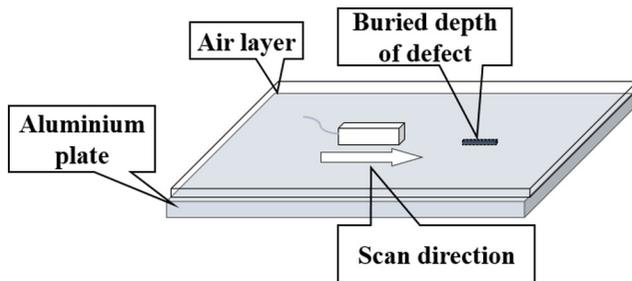

Figure 17 Simulation detection results
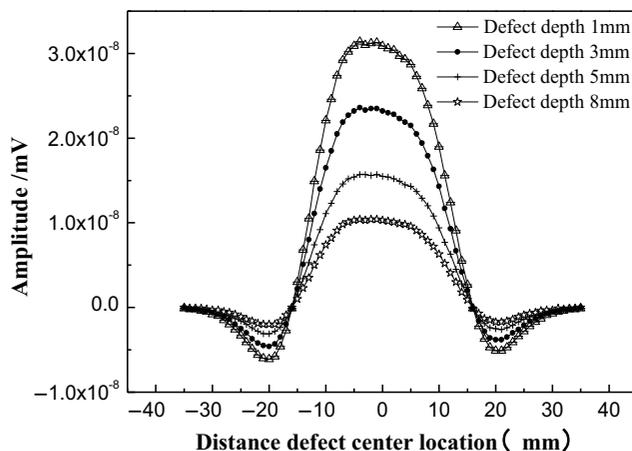
increases sharply. When the excitation coil passes over the crack, the detection signal reaches the peak. The sensor continues to move until the excitation coil is away from the defect. When the detection coil is close to the defect, the amplitude declines slowly until the detection coil passes the crack. As the detection coil leaves the defect, the signal amplitude declines sharply. In summary, the sensor can detect the back defect of the damped aluminum plate in the simulation model.

4.2 Verification test

RFEC sensor and building detection system are manufactured on the basis of a comprehensive analysis of the above simulation results. The detection system (Figure 18) mainly consists of a signal generator, ±5 V DC regulated power

Figure 18 Detection system
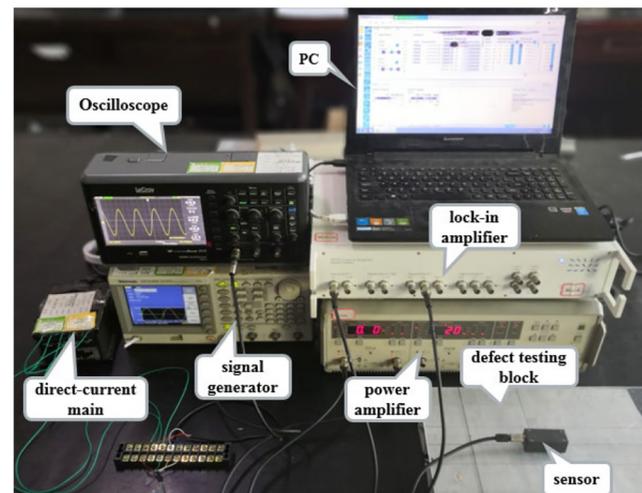
supply, lock-in amplifier, power amplifier, computer, and RFEC sensor. The detection coil picks up the induced voltage signal through the preamplifier for filtering and amplification as the signal generator generates a sine wave signal, which is loaded onto the excitation coil after passing through the power amplifier. Finally, the data are collected through the lock-in amplifier and stored in the computer.

In the detection of the defects of aluminum plate specimens, the thickness of aluminum plate specimens vary at 1, 3, 5, and 8 mm. The defects, which measure 10 mm length × 0.2 mm width × 1 mm depth, are located in the backside of plate specimens. Non-conductive coating is used instead of the damping coating for the experimental study. The plate specimens are scanned using a manufactured sensor. The amplitude of the detection signal is extracted using a lock-in amplifier. The result is shown in Figure 19.

Figure 19 shows that the detection signals of the defects on the backside of aluminum plates are visible. The measurements are 1, 3 and 5 mm. The detection signals reached a peak, which is consistent with the simulation results. As the detection signal displayed is not ideal when it is lifted by 8 mm, the experimental results show that the RFEC sensor can detect the crack defects measuring10 mm length × 0.2 mm width × 1 mm depth on the back surface of the 5 mm aluminum plate in the state of 5 mm thick damping slurry.

To verify the consistency of the simulation and test results, the detection signal amplitudes of different depth defects in the

Figure 19 Test results
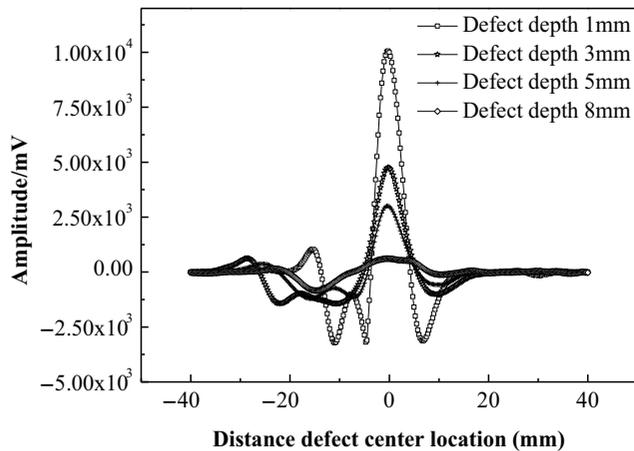
simulation and test results are extracted to ensure that the detection signal amplitudes in the test results remain unchanged. The detection amplitude of the depth defect is used as the benchmark, and the signal amplitudes in the simulation results the values are mapped to the test results, and the comparison results of simulation and test for different depth defects are shown in Figure 20.

It can be seen from Figure 20 that the amplitude of the detection signal decreases as the depth increases, and the simulation result is basically consistent with the experimental result. The detection capability of the RFEC sensor can meet our expectations by evaluating the experimental research. In the state of being lifted 5 mm away, it can still detect 10 mm length $\times$ 0.2 mm width $\times$ 1mm depth crack defects on the rear surface of the 5 mm aluminum plate.

5. Conclusion

1 In this paper, the simulation results show that the inner diameter of the excitation coil is proportional to the

Figure 20 Comparison of simulation and test results of different depth defects
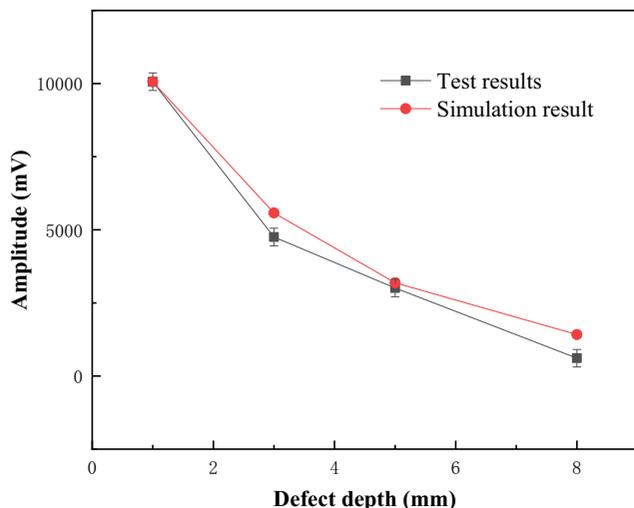
strength of the indirect coupled magnetic field, but the height of the excitation coil is inversely proportional to the indirect coupled magnetic field. Thus, the inner diameter of the excitation coil is increased accordingly, and the height of the excitation coil is reduced to improve the indirect coupled magnetic field in the sensor design process.

2 The ferrite magnetic circuit can guide the magnetic field lines. Thus, increasing the radius of the magnetic cylinder can increase the strength of the excitation magnetic field in the design the magnetic circuit. An increase in radius and height of the magnetic cup can achieve the same effect.

3 Copper cup is used as the direct coupling magnetic field shield structure, which reduces wall thickness, improves indirect coupled magnetic field strength and does not change the location of the remote field point.

4 The excitation frequency is larger than 500 Hz. The location of the remote field point gradually converges. When the excitation frequency is 600 Hz, the remote field point is 30 mm away from the center of the excitation coil.

5 The RFEC is introduced to the field of the coated part detection. 2D and 3D finite element simulation models are established by ANSYS finite element simulation software. The sensor detection capacity improved on two aspects: enhancing the excitation magnetic field and suppressing direct coupling energy, which overcomes the interference caused by the damping coating, and achieving the RFEC detection with the buried depth defect of the damping coating aluminum plate successfully.

References

Askari, M., Taheri, A., Larijani, M.M., Movafeghi, A. and Faripour, H. (2019), "Evaluation of CsI (Na) rod scintillator application in industrial gamma-ray computed tomography", *Nuclear Instruments and Methods in Physics Research Section A: Accelerators, Spectrometers, Detectors and Associated Equipment*, Vol. 941, pp. 162-329.

Chen, P. and Huang, P. (2017), "Detection mechanism and magnetic field distribution characteristics for plate remote-field eddy-current testing", Progress In Electromagnetics Research Symposium-Spring (PIERS*)*, pp. 1898-1905.

Dalton, C.R., Olson, B.W. and Lai, F.C. (2009), "Nondestructive evaluation of surface defects using scanning infrared thermography", *Journal of Thermophysics and Heat Transfer*, Vol. 23 No. 4, pp. 716-724.

Du Plessis, A., Le Roux, S.G. and Guelpaa, A. (2016), "Comparison of medical and industrial X-ray computed tomography for non-destructive testing", *Case Studies in Nondestructive Testing and Evaluation*, Vol. 6, pp. 17-25.

Fan, R., Meng, G., Yang, J. and He, C. (2009), "Experimental study of the effect of viscoelastic damping materials on noise and vibration reduction within railway vehicles", *Journal of Sound and Vibration*, Vol. 319 No. 1-2, pp. 58-76.

Fukutomi, H., Takagi, T. and Nishikawa, M. (2001), "Remote field eddy current technique applied to non-magnetic steam

generator tubes", *NDT & E International*, Vol. 34 No. 1, pp. 17-23.

He, Y., Pan, M., Luo, F. and Tian, G. (2011), "Pulsed eddy current imaging and frequency spectrum analysis for hidden defect nondestructive testing and evaluation", *NDT & E International*, Vol. 44 No. 4, pp. 344-352.

Jayaraman, R., Solomon, S.J., Sridhar, N., Krishnamurthy, V. C. and Arunachalam, K. (2021), "Numerical modelling of remote field eddy current testing of steam generator tubes", *Advances in Non-Destructive Evaluation*, pp. 239-248.

Kasai, N., Matsuzaki, S. and Sakamoto, T. (2011), "Experimental and analytical study for detectability of the back-side flaws of flat ferromagnetic plates by RFECT", *NDT & E International*, Vol. 44 No. 8, pp. 703-707.

Kermadi, M., Moussaoui, S., Brahimi, A.T. and Feliachi, M. (2018), "Defect localization and characterization in eddy current nondestructive testing by change detection and global optimization", *COMPEL – The International Journal for Computation and Mathematics in Electrical and Electronic Engineering*, Vol. 37 No. 2, pp. 948-970.

Ona, D.I., Tian, G. and Sutthaweekul, R. (2019), "Design and optimisation of mutual inductance based pulsed eddy current probe", *Measurement*, Vol. 144, pp. 402-409.

Pokhmurskii, V.I., Zin, I.M., Vynar, V.A. and Bily, L.M. (2011), "Contradictory effect of chromate inhibitor on corrosive wear of aluminium alloy", *Corrosion Science*, Vol. 53 No. 3, pp. 904-908.

Robinson, D. (1998), "Identification and sizing of defects in metallic pipes by remote field eddy current inspection", *Tunnelling and Underground Space Technology*, Vol. 13, pp. 17-27.

She, S., Chen, Y., He, Y., Zhou, Z. and Zou, X. (2021), "Optimal design of remote field eddy current testing probe for ferromagnetic pipeline inspection", *Measurement*, Vol. 168, p. 108306.

Shi, Y., Luo, Q., Wang, Z., Zhang, W. and Li, Y. (2019a), "Dual sensing coils used for RFEC testing of joint casings in oil wells", *Measurement*, Vol. 133, pp. 68-76.

Shi, M., Feng, L., Huang, Z., Zhang, M., Wen, H. and Liu, Q. (2019b), "Defect detection of oil and gas pipeline using remote field eddy current technology(article)", *Journal of Magnetics*, Vol. 24 No. 3, pp. 530-542.

Sophian, A., Tian, G. and Fan, M. (2017), "Pulsed eddy current non-destructive testing and evaluation: a review", *Chinese Journal of Mechanical Engineering*, Vol. 30 No. 3, pp. 500-514.

Sun, Y., Wan, W., Yang, X., Sun, C., Zhu, H. and Ouyang, T. (2008), "Applications of motorized rotational RFEC probes in thick and multilayer structure crack detection", AIP Conference Proceedings, Vol. 975, pp. 336-343.

Thirunavukkarasu, S., Rao, B.P.C., Vaidyanathan, S., Jayakumar, T. and Raj, B. (2008), "Influence of sodium deposits in steam generator tubes on remote field eddy current signals", *International Journal of Pressure Vessels and Piping*, Vol. 85 No. 4, pp. 211-218.

Wang, Y., Gao, X., Finckbohner, M. and Netzelmann, U. (2019), "The effect of paint coatings on detection of vertical surface cracks in metals by induction thermography", *NDT & E International*, Vol. 104, pp. 58-68.

Woo, S., O'Neal, D.L. and Pecht, M. (2010), "Failure analysis and redesign of the evaporator tubing in a kimchi refrigerator", *Engineering Failure Analysis*, Vol. 17 No. 2, pp. 369-379.

Xiao, Q., Xu, Z. and Wu, Q. (2018), "Outside inspection method for carbon steel pipe defects based on remote field eddy current(article)", *Chinese Journal of Sensors and Actuators*, Vol. 31 No. 11, pp. 1684-1689.

Xie, L., Gao, B., Tian, G., Xiao, X., Wu, S., Yin, Y. and Mao, D. (2018), "Investigation of remote field eddy current defect detection for pipeline welds", *IEEE Far East NDT New Technology & Application Forum (FENDT)*, pp. 137-141.

Xu, Z., Lin, Z. and Xiao, Q. (2019), "A remote field eddy current probe for outside inspection of pipe defects", *International Journal of Applied Electromagnetics and Mechanics*, Vol. 59 No. 4, pp. 1543-1551.

Yang, J.H. and Yoon, Y.S. (2001), "Detection of metal defects on gas distribution pipeline by remote field eddy current (RFEC) using Finite-Element analysis", OGST – Oil & gas science and Technology - Revued", *Oil & Gas Science and Technology*, Vol. 56 No. 2, pp. 161-179.

Yang, B., Xu, J., Wang, X. and Cao, H. (2017a), "Research on remote field eddy current technique applied to inspect riveted structure", *Chinese Journal of Sensors and Actuators*, Vol. 30 No. 10, pp. 1493-1496.

Yang, B., Xu, J., Wu, H. and He, Y. (2017b), "Magnetic field shielding technique for pulsed remote field eddy current inspection of planar conductors", *NDT & E International*, Vol. 90, pp. 48-54.

Yano, D., Ishikawa, S., Tanaka, K. and Kijimoto, S. (2019), "Vibration analysis of viscoelastic damping material attached to a cylindrical pipe by added mass and added damping", *Journal of Sound and Vibration*, Vol. 454, pp. 14-31.

Zhao, B., Song, K., Ning, N., Huang, H. and Zhang, L. (2020), "Optimization and experimentation of remote field eddy current testing probe for hidden defects of aircraft riveting parts(article)", *Hangkong Xuebao/Acta Aeronautica et Astronautica Sinica*, Vol. 41 No. 1.

Corresponding author

Kai Song can be contacted at: yifulou211@163.com